Journal of
Applied Crystallography
ISSN 0021-8898
Editor: **Anke R. Kaysser-Pyzalla**

Three-dimensional reconstruction of liquid phases in disordered mesopores using *in situ* small-angle scattering

Cedric J. Gommes

J. Appl. Cryst. (2013). **46**, 493–504

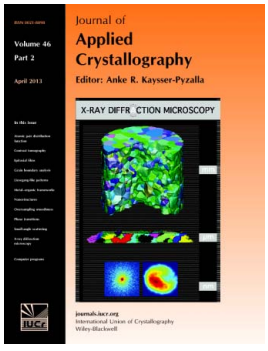

Journal of Applied Crystallography covers a wide range of crystallographic topics from the viewpoints of both techniques and theory. The journal presents papers on the application of crystallographic techniques and on the related apparatus and computer software. For many years, the *Journal of Applied Crystallography* has been the main vehicle for the publication of small-angle scattering papers and powder diffraction techniques. The journal is the primary place where crystallographic computer program information is published.

Journal of
Applied Crystallography
ISSN 0021-8898

Received 8 September 2012
Accepted 7 February 2013

Three-dimensional reconstruction of liquid phases in disordered mesopores using *in situ* small-angle scattering

Cedric J. Gommes

Department of Chemical Engineering, University of Liège B6 A, 3 allée du 6 août, B-4000 Liège, Belgium, and Department of Chemistry, Katholieke Universiteit Leuven, Celestijnenlaan 200F, B-3001 Heverlee, Belgium. Correspondence e-mail: cedric.gommes@ulg.ac.be

Small-angle scattering of X-rays (SAXS) or neutrons is one of the few experimental methods currently available for the *in situ* analysis of phenomena in mesoporous materials at the mesoscopic scale. In the case of disordered mesoporous materials, however, the main difficulty of the method lies in the data analysis. A stochastic model is presented, which enables one to reconstruct the three-dimensional nanostructure of liquids confined in disordered mesopores starting from small-angle scattering data. This so-called plurigaussian model is a multi-phase generalization of clipped Gaussian random field models. Its potential is illustrated through the synchrotron SAXS analysis of a gel permeated with a critical nitrobenzene/hexane solution that is progressively cooled below its consolute temperature. The reconstruction brings to light a wetting transition whereby the nanostructure of the pore-filling liquids passes from wetting layers that uniformly cover the solid phase of the gel to plugs that locally occlude the pores. Using the plurigaussian model, the dewetting phenomenon is analyzed quantitatively at the nanometre scale in terms of changing specific interface areas, contact angle and specific length of the triple line.

1. Introduction

A multitude of technologies and chemical processes make use of mesoporous materials: heterogeneous catalysis, including electrochemical reactions in fuel-cell electrodes, adsorption separation processes and kinetically selective membrane processes are but a few examples. Mesopores are also relevant to natural processes as diverse as the weathering of rocks and ion transport through biological membranes. The unique physicochemical properties of nanometre-scale systems – large surface-to-volume ratios, dominant role of dispersive forces (Van Honschoten *et al.*, 2010), Gibbs–Thomson effects (Zhang *et al.*, 2007), metastability (Chen *et al.*, 1997), thermal fluctuations (Hänggi & Marchesoni, 2009), quantum confinement (Häkkinen *et al.*, 2003) *etc*. – potentially play a prominent role in all applications of mesoporous materials (Schoonheydt & Weckhuysen, 2009). This can lead to extremely counterintuitive phenomena (Nguyen *et al.*, 2010), many of which have been predicted theoretically but are still awaiting experimental confirmation (Harish *et al.*, 2008). The availability of a general method to reconstruct *in situ* the nanostructure of phases confined inside mesoporous solids would be invaluable to researchers in all these fields.

Numerous methods are available for the *ex situ* characterization of nanostructures, the most common being electron microscopy and tomography (Midgley & Dunin-Borkovski, 2009; Friedrich *et al.*, 2009). However, electron microscopy can be used only exceptionally for *in situ* studies, for analyzing some phenomena occurring at extremely low pressure (Simonsen *et al.*, 2010, 2011). General experimental methods that can be used on porous materials for *in situ* studies with nanometre resolution are scarce. Most experimental methods are macroscopic, such as vapor adsorption measurements (Neimark & Ravikovitch, 2001), intrusion porosimetry (Galarneau *et al.*, 2008), electric measurements (Powell *et al.*, 2011) *etc*. On the other hand, spatially resolved methods either have a resolution much larger than the pore size [*e.g*. light microscopy (Okamoto *et al.*, 2004) and micro-imaging (Zhang *et al.*, 2009)] or can only track individual molecules. Nuclear magnetic resonance (Valiullin *et al.*, 2011), neutron spin echo (Kusmin *et al.*, 2010) and single-molecule microscopy (Lebold *et al.*, 2009) belong to the latter category. However, if one wants to understand fully the properties of matter in nanopores it is necessary to investigate the collective behavior of a large number of molecules on a mesoscopic scale comparable to the pore size. On length scales relevant to mesoporous materials, *i.e*. with pore size from 2 to 50 nm, small-angle scattering (SAS) of X-rays (SAXS) or neutrons (SANS) is close to being the only option (Glatter & Kratky, 1982; Sinha, 1999).

Small-angle scattering can in principle be used to analyze any type of nanostructure, provided there is a sufficient contrast between the various phases. SAS is also very flexible

experimentally (Koch & Bras, 2008): measurements can be done over a wide range of temperature and pressure (Mitchell *et al.*, 2008), in a variety of chemical environments and often in a variety of working conditions (Marco & Veder, 2010). Moreover, in the case of synchrotron SAS, time-resolved measurements are possible with a resolution as low as a few milliseconds (Henzler *et al.*, 2008). The latter time resolution is constantly being improved through the development of more efficient detectors as well as more intense X-ray sources, most notably free-electron lasers (Emma *et al.*, 2010). However, in the case of mesoporous materials with a complex structure, the huge potential of SAS is considerably hindered by a nearly complete lack of data analysis methods to reconstruct real-space structures from scattering data.

Recently, the main difficulties pertaining to SAS data analysis in disordered porous materials have been circumvented through the use of ordered mesoporous materials (Ciesla & Schüth, 1999) for *in situ* studies (Hofmann *et al.*, 2005; Mascotto *et al.*, 2010; Lefort *et al.*, 2011). However, there is increasing evidence that structural disorder plays a crucial role in determining the properties of matter confined in mesopores (Wallacher *et al.*, 2004; Bonnet *et al.*, 2008). Slight deviations from geometrical ideality can act as nucleation sites and trigger phase transitions that would otherwise take place under different circumstances (Gommes, 2012). Moreover, the choice of a material for any practical application generally results from a compromise between several different properties, and having an ordered structure is never one of them (Rolison, 2003; Gelb, 2009). Therefore, the problem of SAS data analysis in disordered mesopores has to be addressed for any *in situ* study of practical relevance.

In the present paper we introduce a general mathematical method for the three-dimensional reconstruction of phases dispersed in disordered mesoporous materials, starting from *in situ* SAS data. The method is based on so-called plurigaussian stochastic models (Armstrong *et al.*, 2003), which are a multi-phase generalization of clipped Gaussian random field models that have been widely used to analyze the structure of emulsions (Teubner, 1991), porous glass (Levitz, 1998), polymer blends (Jinnai *et al.*, 1997; D'Hollander *et al.*, 2010) and gels (Gommes & Roberts, 2008).

We illustrate the potential of plurigaussian modeling by applying it to the *in situ* analysis of partially miscible liquids confined in nanopores. Liquid–liquid equilibria under confinement are of interest for a host of applications related to separation technologies, to oil recovery, to lubrication and to coating. The numerous papers published about that topic since the late 1980s testify both to the importance of the field and to unsettled theoretical debates (see Gelb *et al.*, 1999, and references therein). The competing theories about liquid–liquid equilibria put a different emphasis on the randomness of the confining porous medium, on critical fluctuations and how they are affected by the pore size, and on macroscopic concepts pertaining to wetting phenomena, the very relevance of which is unclear at the nanometre scale. The latter concepts, in particular, predict a variety of possible morphologies for confined liquids – adsorbed layers, capsules floating in the middle of the pores or isolated plugs – depending on subtle equilibria between dispersive forces and surface tension (Liu *et al.*, 1990; Monette *et al.*, 1992). The difficulty in settling these debates despite the numerous experimental SAS studies (Lin *et al.*, 1994; Frisken *et al.*, 1995; Formisano & Teixeira, 2000; Hellweg *et al.*, 2003; Schemmel *et al.*, 2005) results from the lack of a data analysis method that would enable one to use data of this type to reconstruct the nanostructure of the confined liquids.

The specific system we investigate here is a resorcinol formaldehyde (RF) gel permeated with a critical hexane/nitrobezene binary solution. The choice of RF materials is motivated by several factors. First, they are purely mesoporous, which contrasts with other possible materials such as controlled porous glass, the surface of which is often described as a surface fractal (Mitropoulos *et al.*, 1997; Levitz, 1998). Second, their nanostructure has already been characterized thoroughly by a variety of techniques (Pekala & Schaefer, 1993; Al-Muhtaseb & Ritter, 2003; Gommes & Roberts, 2008), which makes them a suitable model of disordered mesoporous materials. Last but not least, calcined RF aerogels are promising materials for catalysis applications, notably as fuel cell electrodes (Ouattara-Brigaudet *et al.*, 2012). The present work therefore paves the way to more complex studies of technological relevance such as the mesoscopic analysis of water production in working RF-based fuel cell cathodes.

2. Experimental

2.1. Sample preparation

The RF gel was synthesized *via* the polycondensation of resorcinol and formaldehyde in water with sodium carbonate as a basification agent, as fully described elsewhere (Job *et al.*, 2005). The resorcinol/formaldehyde molar ratio was set to 0.5. The dilution molar ratio water/(resorcinol + formaldehyde + sodium carbonate) was set to 6, and the resorcinol/sodium carbonate molar ratio was set to 150. The resulting gel was aged for three days at 343 K in a closed vial.

Based on the composition of the starting solution, the solid fraction of the gel is estimated to be 25 vol.%. This estimation results from assuming that the reaction is complete, which leads to an overall stoichiometry of $C_8H_{7.33}O_{2.66}$ for the solid phase of the gel (Al-Muhtaseb & Ritter, 2003), and from the known density $\rho_m \simeq 1.5$ g ml^{-1} of the solid phase of the gel measured by helium pycnometry on the desiccated gel (Job *et al.*, 2005).

The mother solvent of the gel (mostly water) was exchanged for a critical hexane/nitrobenzene solution. Since neither hexane nor nitrobenzene is soluble in water, acetone was used as an intermediate solvent. The gel was cut into small cubes, 1 nm in size, which were washed overnight in a large excess of acetone and subsequently in a large excess of a critical hexane/nitrobenzene solution, *i.e.* having 42.2 mol% nitrobenzene. The latter step was repeated three times. An RF gel with pores permeated with pure nitrobenzene was prepared in the same way.

There is a slight experimental uncertainty on the global composition of the pore-filling liquid. Indeed, the SAXS analysis shows that nitrobenzene adsorbs on the surface of the solid, which increases the overall nitrobenzene concentration in the pores of the gel compared to the supernatant solution. The composition of the supernatant converts to 36 vol.% nitrobenzene and 64 vol.% hexane assuming volume conservation. For the SAXS data analysis we have assumed that the global composition of pore-filling liquid is 50:50 vol.%. However, the results remain qualitatively unchanged if slightly different values are used, as we discuss further later.

2.2. Small-angle scattering

The SAXS measurements were conducted at the Dutch–Belgian station, BM26, of the European Synchrotron Radiation Facility (Grenoble, France). The SAXS patterns were measured on a two-dimensional multiwire gas-filled detector placed at 5 m from the sample.

A millimetre-sized piece of gel was taken out of the supernatant solution and presented in hermetically closed aluminium pans (Perkin–Elmer, Waltham, MA, USA). The temperature was controlled using a Linkam HFS 191 heating/freezing stage. The SAXS measurements were performed while the sample was cooled from 303 to 213 K at a rate of 5 K min^{-1}. The acquisition time was set to 12 s, which corresponds to one pattern per kelvin.

The intensity was normalized to the intensity of the transmitted beam, measured by a photodiode placed on the detector beamstop, and corrected for the detector response. The isotropic two-dimensional scattering patterns were averaged azimuthally using custom-made software (Gommes & Goderis, 2010) and expressed as a function of the scattering vector modulus

$$q = (4\pi/\lambda)\sin(2\theta/2), \qquad (1)$$

with λ being the wavelength (0.95 Å in the used setup) and 2θ the scattering angle. Finally, the patterns were corrected for the scattering due to the empty setup, taking account of the sample and sample holder transmissions.

The SAXS pattern of the RF gel used in the present work is shown in Fig. 1 as the scattering intensity I against scattering vector magnitude q. For practical reasons the pattern was measured with pores of the gel permeated with pure nitrobenzene. We shall come shortly to the thorough structural analysis of the data and we only mention here that the pattern is typical of disordered mesoporous materials. It has a broad maximum around $q \simeq 0.03$ Å^{-1}, which corresponds to a characteristic length $2\pi/q \simeq 20$ nm. The latter length can be thought of as an approximate pore size for the present type of low-density material (Roberts, 1997). When the temperature is lowered to 258 K the SAXS patterns change minimally, as a result of thermal contraction of both the nitrobenzene and the solid phase. In the rest of the paper, we consider the pattern in Fig. 1 as representative of the solid nanostructure of the gel over the entire investigated temperature range.

Fig. 2 shows the SAXS intensity measured on the RF gel permeated with the critical binary nitrobenzene/hexane solution, when the temperature is lowered from 303 to 243 K. The SAXS patterns are initially qualitatively similar to that in Fig. 1. Some extra scattering appears at low angles when the temperature is lowered below 288 K, which points to structural changes in the system at the nanometre scale. The evolution exhibits no sharp transition and it is continuous until the temperature of 258 K is reached. Below that temperature,

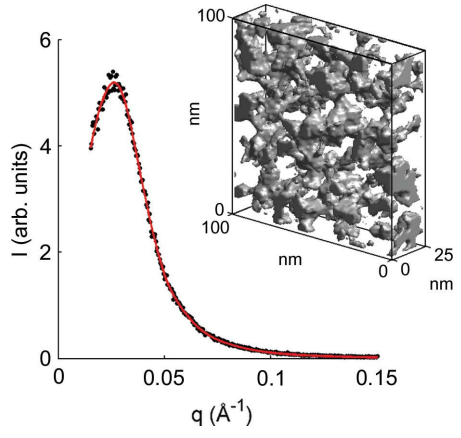

Figure 1
SAXS pattern of the (RF) gel (filled circles) permeated with pure nitrobenzene, and its reconstructed nanostructure as a clipped Gaussian random field. The solid red line is the SAXS pattern of the reconstruction.

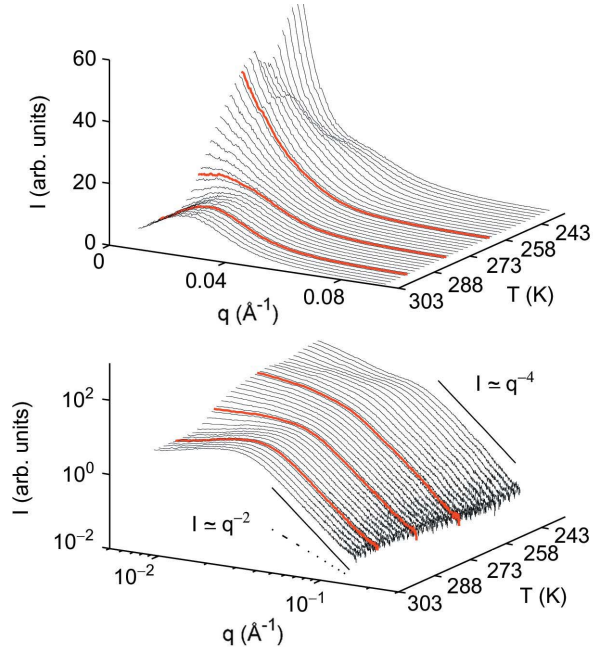

Figure 2
Small-angle X-ray scattering patterns of the RF gel permeated with critical nitrobenzene/hexane solution, during cooling from 303 to 243 K. The same data are plotted in the top and bottom graphs on linear and logarithmic scales, respectively. The two solid lines in the bottom graph are Porod scattering of the type $I \simeq q^{-4}$, and the dashed line is the $I \simeq q^{-2}$ scattering relevant to concentration fluctuations. The three temperatures highlighted in red are 293, 278 and 259 K, which are analyzed further in Fig. 5.

the Bragg peaks of solid nitrobenzene appear in the wide-angle scattering (see Fig. SI-1 in the supporting information[1]). We shall focus our analysis on temperatures higher than 258 K, for which all pore-filling phases are liquid.

Observations qualitatively similar to those of Fig. 2 have been reported for other nanoporous solids permeated with binary solutions. These data have been analyzed either in terms of concentration fluctuations in the pore-filling binary solutions, the amplitude of which increases when the critical point is approached (Frisken *et al.*, 1995; Formisano & Teixeira, 2000; Hellweg *et al.*, 2003), or in terms of liquid–liquid phase separation whereby a nanoemulsion forms inside the pores of the material, starting from a homogeneous binary solution (Lin *et al.*, 1994; Schemmel *et al.*, 2005). Interestingly, both scenarios can be ruled out in the present case. Indeed, the intensity of X-rays scattered by statistical concentration fluctuations is expected to decrease asymptotically as $I \simeq q^{-2}$ for large values of q (Glatter & Kratky, 1982). Although such a trend could be present for very large values of q (Fig. 2, bottom), the SAXS patterns are dominated at large q by a so-called Porod scattering, with $I \simeq q^{-4}$, which points to a nanostructure with sharp interfaces (Glatter & Kratky, 1982). The deviation of the data from Porod scattering is made quantitative by fitting the data for $q \geq 0.1$ Å^{-1} by

$$I(q) = I_{\rm BG} + Aq^{-4}, \tag{2}$$

where the values of the constants $I_{\rm BG}$ and A are determined by least squares. The values of $I_{\rm BG}$ contribute to the discussion section.

In addition to the critical fluctuations scenario, the phase separation scenario has to be ruled out. This results from considering the values of Porod's invariant Q, calculated as

$$Q = \int_0^\infty I(q)\, 4\pi q^2\, {\rm d}q, \tag{3}$$

after extrapolating $I(q)$ at high q with a q^{-4} Porod scattering. The values obtained from the SAXS data of Fig. 2 are plotted in Fig. 3, and they are found to be remarkably constant. The increase of Q below 258 K results from the crystallization of the nitrobenzene, but we shall not investigate that temperature range in the present work. We show in the supporting information that a phase separation in the present system would be accompanied by a more than 50% increase of Q. The process observed in Fig. 2 is therefore a morphological transition: the evolution of the SAXS data corresponds mostly to a reorganization of existing phases within the pores of the RF material. However, the nature and spatial distribution of the phases inside the pores are unknown at this stage.

3. Data analysis and modeling

In order to gain qualitative insight into the nanostructure of the pore-filling phases it is necessary to analyze quantitatively the SAXS patterns. Quite generally, the SAXS intensity is proportional to the Fourier transform of the electron density correlation function,

$$I(q) = K \int_0^\infty \frac{\sin(qr)}{qr} C(r)\, 4\pi r^2\, {\rm d}r, \tag{4}$$

where K is a constant that depends notably on the volume of the sample that is irradiated and $C(r)$ is defined as

$$C(r) = \langle (\rho(\mathbf{x}+\mathbf{r}) - \langle\rho\rangle)(\rho(\mathbf{x}) - \langle\rho\rangle)\rangle. \tag{5}$$

In this equation, $\rho(\mathbf{x})$ is the electron density at point $\mathbf{x}$, and the brackets $\langle\ldots\rangle$ stand for the average value, calculated over all possible $\mathbf{x}$. When expressing $I(q)$, we have assumed that the sample is statistically isotropic, so that $C(\mathbf{r})$ depends only on the modulus $r = |\mathbf{r}|$.

When analyzing the scattering by phases confined in nanopores it is necessary to consider at least three phases, namely the solid phase S and the two pore-filling phases A and B. In our particular case, phases A and B are the nitrobenzene-rich and hexane-rich phases, respectively. The electron density correlation function can then be written as

$$\begin{aligned} C(r) = {} & (\rho_S - \rho_A)(\rho_S - \rho_B)\big[P_{SS}(r) - \phi_S^2\big] \\ & + (\rho_A - \rho_S)(\rho_A - \rho_B)\big[P_{AA}(r) - \phi_A^2\big] \\ & + (\rho_B - \rho_S)(\rho_B - \rho_A)\big[P_{BB}(r) - \phi_B^2\big], \end{aligned} \tag{6}$$

where ϕ_S, ϕ_A and ϕ_B are the volume fractions of the corresponding phases, and the functions $P_{SS}(r)$, $P_{AA}(r)$ and $P_{BB}(r)$ are the two-point correlation functions of phases S, A and B (Debye *et al.*, 1957; Ciccariello *et al.*, 1981; Torquato, 2000). These functions can be thought of as the probability that two points randomly chosen in the system at distance r from each other both belong to phase S, A or B, respectively. In the particular case where the pores are filled with a single phase, as is relevant to the SAXS data in Fig. 1, the electron correlation function $C(r)$ is simply proportional to $P_{SS}(r)$, as it should be.

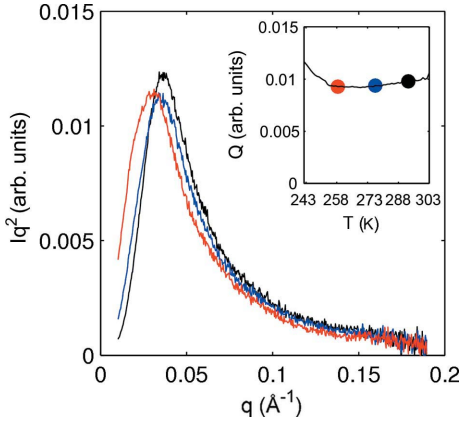

Figure 3
Kratky plots corresponding to the SAXS data of Fig. 2, whereby $I\,q^2$ is plotted against q. The inset shows Porod's invariant Q calculated from the area under the curves. The three temperatures are 293 K (black), 278 K (blue) and 259 K (red).

[1] Supplementary material is available from the IUCr electronic archives (Reference: CE5149). Services for accessing this material are described at the back of the journal.

From a previous SAXS analysis of RF gel formation (Gommes & Roberts, 2008), the structure of the solid phase of the gel is known to be accurately described by a so-called clipped Gaussian random field (GRF) model (Joshi, 1974; Quiblier, 1984; Berk, 1987; Teubner, 1991; Levitz, 1998). A GRF $Y(\mathbf{x})$ can be thought of as the superposition of a large number of wave-like sinusoidal functions, such as

$$Y(\mathbf{x}) = (2/N)^{1/2} \sum_{n=1}^{N} \sin(\mathbf{q}_n \cdot \mathbf{x} - \varphi_n), \tag{7}$$

where $\mathbf{q}_n$ are wavevectors that are random in both orientation and magnitude, and φ_n are random phases uniformly distributed in the interval $[0, 2\pi)$. The values of Y obtained in this way for any $\mathbf{x}$ are Gaussian distributed with average value 0, and the factor $(2/N)^{1/2}$ ensures that the variance is equal to 1. A GRF is therefore completely characterized by its power spectral density $f_Y(\mathbf{q})$, which is equivalent to the statistical distribution from which the vectors $\mathbf{q}_n$ are drawn. In the particular case of an isotropic GRF, the field correlation function $g_Y(r) = \langle Y(x)Y(x+r)\rangle$ is related to $f_Y(q)$ through

$$g_Y(r) = \int_0^\infty f_Y(q) \frac{\sin(qr)}{qr} 4\pi q^2 \mathrm{d}q. \tag{8}$$

Examples of two GRFs, $Y(\mathbf{x})$ and $Z(\mathbf{x})$, obtained with different power spectral densities $f_Y(q)$ and $f_Z(q)$ are shown in Fig. 4.

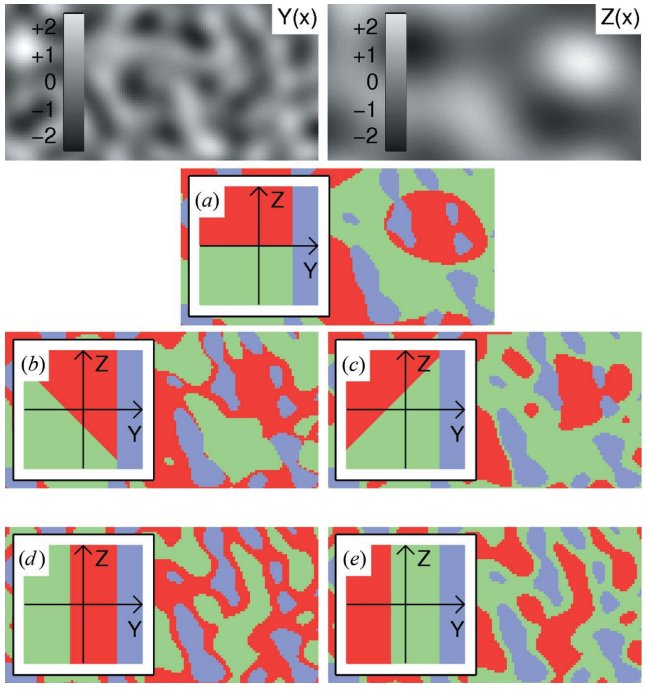

Figure 4
Plurigaussian modeling of the nanostructure of the RF gel with pores filled by hexane-rich and nitrobenzene-rich phases. Two independent Gaussian random fields $Y(\mathbf{x})$ and $Z(\mathbf{x})$ are used, and each phase is modeled as a particular region of the (Y, Z) plane. (*a*)–(*e*) Different nanostructures obtained from Y and Z: the main figures are the real-space nanostructures and the insets are the corresponding regions of the (Y, Z) plane. The solid phase is shown in gray, the nitrobenzene phase in red and the hexane phase in green.

The solid phase of the gel is modeled here as the points of space where $Y(\mathbf{x})$ takes values larger than a given threshold a. Because $Y(\mathbf{x})$ is Gaussian distributed, the threshold a is related to the volume fraction of the gel ϕ_S through the following error function:

$$\phi_S = \int_a^\infty \frac{1}{(2\pi)^{1/2}} \exp\left(-\frac{t^2}{2}\right) \mathrm{d}t. \tag{9}$$

The known value $\phi_S = 0.25$ converts to a threshold $a = 0.67$. The two-point correlation function is calculated as (Teubner, 1991)

$$P_{SS}(\mathbf{r}) = \phi_S^2 + \frac{1}{2\pi} \int_0^{g_Y(r)} \frac{1}{(1-t^2)^{1/2}} \exp\left(-\frac{a^2}{1+t}\right) \mathrm{d}t, \tag{10}$$

which enables one to use clipped GRF models to analyze SAXS data. The reconstruction shown as the inset of Fig. 1 was obtained by optimizing the power spectral density $f_Y(q)$ so as to match the experimental SAXS data, following the procedure of Quintanilla & Jones (2007). The physical reason for the accuracy of this geometrical model for RF gels is that their nanostructure forms *via* a spinodal decomposition process (Schaefer *et al.*, 1995; Gommes *et al.*, 2008), which is governed by equations very similar to those of Gaussian random fields (Cahn, 1965).

When the pores of the gel are not filled with a single homogeneous phase, the nanostructure of the pore-filling phases A and B contributes also to the SAXS intensity through the functions $P_{AA}(r)$ and $P_{BB}(r)$ in equation (6), and a geometrical model is needed for these phases as well. The model we use here is a so-called plurigaussian model, which is a generalization of the clipped GRF model used in Fig. 1. Plurigaussian models have been introduced in the context of geological engineering (Le Loc'h & Galli, 1999; Armstrong *et al.*, 2003), but to the best of our knowledge they have never been used to analyze SAS data. In the particular version of the model that we propose, two independent GRFs $Y(\mathbf{x})$ and $Z(\mathbf{x})$ are combined as illustrated in Fig. 4. The possible values taken by the two fields at any given point $\mathbf{x}$ can be represented in a (Y, Z) plane: in this context a given phase i is modeled as a domain D_i of the (Y, Z) plane. In other words, a point $\mathbf{x}$ belongs to phase i if the values taken by the two fields at point $\mathbf{x}$ satisfy $[Y(\mathbf{x}), Z(\mathbf{x})] \in D_i$. It has to be noted that the standard clipped GRF model used to reconstruct the solid phase of the RF gel in Fig. 1 is a particular case of this plurigaussian model, where the (Y, Z) domain of the solid phase D_S is a half-plane with boundary parallel to the Z axis (displayed in gray in Fig. 4). The model we shall use for the pore-filling phases is the simplest possible: the region of the (Y, Z) plane complementary to D_S is simply cut into two regions by a straight line. This defines the two domains D_A and D_B corresponding to the nitrobenzene-rich and hexane-rich phases.

Despite its conceptual simplicity, the plurigaussian model can account for a variety of nanostructures of the pore-filling phases, depending on the orientation and position of the A/B

boundary line in the (Y, Z) plane. If the boundary is parallel to the Z axis, one phase – either phase A or phase B – is a layer that covers entirely the surface of the solid, and the other phase occupies the remainder of the pore space (Figs. 4*d* and 4*e*). By contrast, if the boundary is parallel to the Y axis, phases A and B are statistically independent of the solid phase (Fig. 4*a*). In this case, phases A and B are simply obtained by clipping the field $Z(\mathbf{x})$ and limiting the phases to within the pore space. For intermediate orientations of the A/B boundary line (Figs. 4*b* and 4*c*), some correlation exists between the nanostructure of the pore-filling phases and that of the solid. In the case of Fig. 4(*b*) the solid phase is made A-philic and B-phobic, and the reciprocal is true for Fig. 4(*c*).

In order to analyze the SAXS data in Fig. 2 with a plurigaussian model, we shall assume that the structure of the solid phase S of the gel does not depend on the temperature and that it is identical to the one reconstructed from the gel permeated with pure nitrobenzene (Fig. 1). Practically, this implies that the (Y, Z) domain of the solid phase is the half-plane where $Y \geq a$ with $a = 0.67$, and that the power spectral density $f_Y(q)$ of field Y is the one obtained previously. The only geometrical parameters left to characterize entirely the pore-filling phases are therefore the two parameters necessary to define the A/B boundary in the (Y, Z) plane and the power spectral density of the Gaussian random field Z, or equivalently its correlation function $g_Z(r)$. For the latter, it proved sufficient to model it as

$$g_Z(r) = \exp\left[-(r/l_Z)^2\right], \tag{11}$$

which introduces a single parameter l_Z having the meaning of a characteristic length. The particular form of equation (11) satisfies the necessary condition that $g_Z(r)$ should be quadratic for small values of r (Berk, 1991). Another simple function having that property is $g_Z(r) = 1/\cosh(r/l_Z)$, which differs significantly from equation (11) for large values of r. The latter function was notably used by Gommes & Roberts (2008), but equation (11) was chosen here because it enabled us to fit the SAXS data more accurately. The nanostructure of the pore-filling phases is therefore entirely specified through only three independent parameters, namely, l_Z and the two parameters that define the A/B boundary line in the (Y, Z) plane.

The structural characteristics of phases A and B are entirely specified through the statistical properties of the fields $g_Y(r)$ and $g_Z(r)$ [or equivalently $f_Y(q)$ and $f_Z(q)$] and through the domains $D_{A/B}$. In particular, the volume fraction of phase A is calculated as

$$\phi_A = \iint_{(y,z)\in D_A} (1/2\pi)\exp\left[-(y^2+z^2)/2\right] \mathrm{d}y\,\mathrm{d}z, \tag{12}$$

and an equivalent relation holds for ϕ_B. The two-point correlation function $P_{AA}(r)$ is

$$P_{AA}(r) = \int_{D_A} \mathrm{d}y_1 \mathrm{d}z_1 \int_{D_A} \mathrm{d}y_2\,\mathrm{d}z_2\, G_{g_Y(r)}(y_1, y_2)\, G_{g_Z(r)}(z_1, z_2), \tag{13}$$

where $G_g(x_1, x_2)$ is the bivariate Gaussian distribution with mean 0, variance 1 and covariance g (Lantuéjoul, 2000). A similar relation holds for $P_{BB}(r)$. The way in which equation (13) is practically evaluated to fit the SAXS data is reported in Appendix *A*.

In addition to the structural parameters discussed so far, a characteristic of the pore-filling phases that is *a priori* unknown is their actual composition. The constancy of Porod's invariant Q suggests that their volume fractions ϕ_A and ϕ_B and their composition are approximately constant but they need not be pure hexane and pure nitrobenzene. A useful approximation for analyzing SAXS data with phases having a changing composition is that of volume conservation (Gommes *et al.*, 2010). Making that assumption, the composition of phases

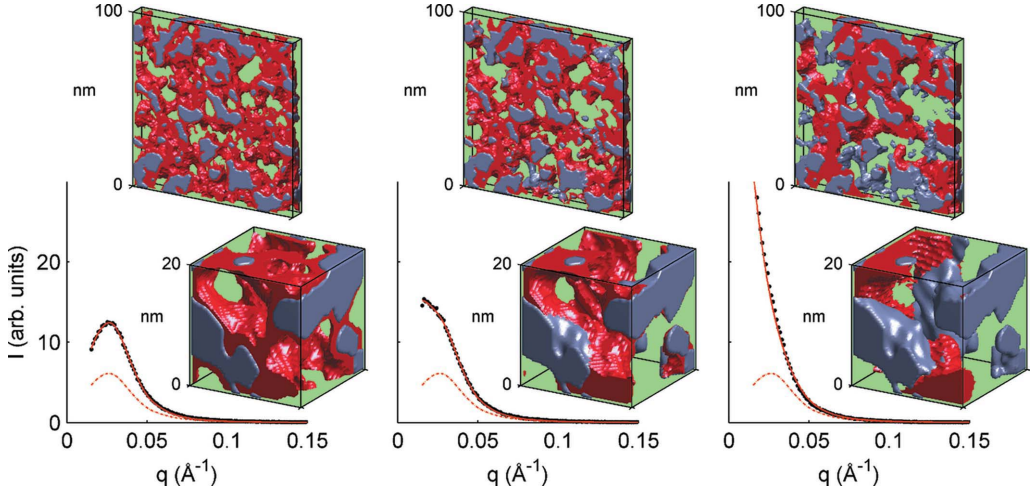

Figure 5
Reconstructed nanostructure of the nitrobenzene/hexane phases inside the pores of the RF gel, at 293, 278 and 259 K (from left to right, corresponding to the temperatures highlighted in Figs. 2 and 3). The solid phase is in gray, the nitrobenzene phase is in red and the hexane phase is symbolized by the green background. Two reconstructions are shown at each temperature, corresponding to two different scales. The experimental SAXS patterns are shown (filled circles) together with the SAXS curves of the reconstructions (red line); the theoretical SAXS curve of the solid filled with a homogeneous hexane/nitrobenzene solution is displayed for comparison (dotted red line).

A and B is entirely specified through the four volume fractions x_N^A, x_N^B, x_H^A and x_H^B, corresponding to the fraction of phase A/B comprising nitrobenzene (N) or hexane (H), respectively. With these notations, the electron densities of the two phases are written as

$$\rho_A = \left(\rho_N x_N^A + \rho_H x_H^A\right)/\left(x_N^A + x_H^A\right),$$
$$\rho_B = \left(\rho_N x_N^B + \rho_H x_H^B\right)/\left(x_N^B + x_H^B\right), \quad (14)$$

where ρ_H and ρ_N are the electron densities of pure hexane and nitrobenzene. Not all the volume fractions $x_{N/H}^{A/B}$ are independent, however, because the global composition of the pore-filling liquid is known (50% nitrobenzene and 50% hexane in volume) and the volume fraction of each phase is fixed by the plurigaussian parameters. We show in the supporting information that the composition of phases A and B is entirely specified through a single additional parameter. When this parameter is left free, the fitting of the SAXS data systematically leads to the value for which the volume of nitrobenzene in phase A is the maximum compatible with the global composition of the pore-filling liquid. For the rest of the analysis, this parameter was therefore fixed to its largest permissible value.

The SAXS data in Fig. 2 were therefore fitted with a total of three adjustable parameters for each temperature. The values of the parameters are reported in Fig. SI-4 of the supporting information. A single value for the normalization constant K that appears in equation (4) is determined for the entire temperature range. Fig. 5 displays realizations of the plurigaussian model using the parameters derived from SAXS. At high temperature, the nitrobenzene phase A forms a nanometre-thin layer that covers uniformly the surface of the solid. It is noteworthy that in this configuration there is no contact between the solid and hexane phases. A dewetting transition is observed when the temperature is decreased, through which the nanostructure of the nitrobenzene phase progressively changes from a layer to a collection of isolated plugs that locally extend over the entire pore section. When the temperature is further decreased, a coarsening process is observed, whereby the number of plugs decreases and their size increases. This is visible in the large-scale reconstructions shown at the top of Fig. 5.

The volume fraction of phase A obtained from the SAXS data is given in Fig. 6 as a function of temperature. At 303 K the nitrobenzene-rich phase A occupies about 40 vol.% of the total pore space, which means that approximately 10% of the nitrobenzene is still dissolved in the hexane-rich phase B. When the temperature is decreased, however, the volume of phase A increases at the expense of the benzene present in phase B. At 263 K the pore-filling phases have reached 50:50 vol.%, which means that the phase separation is complete. These results remain qualitatively unchanged when a slightly different global composition is assumed for the pore-filling liquid. Independently of the imposed global composition, one finds that phase B contains a small quantity of nitrobenzene at 303 K and that the phase separation is complete only at around 258 K.

This qualitative conclusion is confirmed by the analysis of scattering by statistical concentration fluctuations. In binary liquids, the local electron density necessarily deviates from the average value through statistical concentration fluctuations, leading to a SAXS intensity proportional to q^{-2} (Glatter & Kratky, 1982; Formisano & Teixeira, 2000). This contribution is absent in pure liquids. The SAXS data in Fig. 2 clearly deviate from the Porod q^{-4} scattering at large values of q. The deviation, referred to as I_{BG}, is plotted in Fig. 6. The quantity I_{BG} is constant at high temperature and it starts decreasing around 283 K, *i.e.* at the same temperature where the nitrobenzene demixes completely from the hexane according to the plurigaussian analysis. The absence of background scattering at 263 K hints at the presence of pure liquids, and it is therefore an independent confirmation that the phase separation is complete at that temperature.

4. Discussion and conclusions

Strictly speaking, the reconstructions shown in Fig. 5 are particular realizations of the plurigaussian stochastic model with statistical properties identical to the measured system.

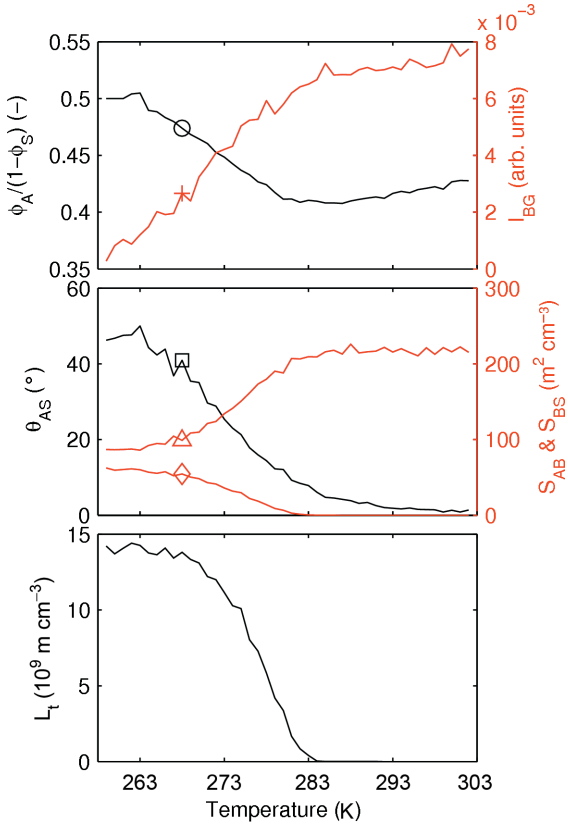

Figure 6
Structural characteristics derived from the SAXS data: (top) fraction $\phi_A/(1-\phi_S)$ of the pore space occupied by the nitrobenzene-rich phase (open circle), and background scattering intensity I_{BG} (plus mark); (middle) interface area S_{AB} (open triangle) and S_{BS} (diamond) between the hexane-rich and nitrobenzene-rich phases and the solid, respectively; contact angle θ_{AS} (open square) between the nitrobenzene-rich phase and the solid; (bottom) specific length L_t of the triple line where phases A, B and S touch each other.

The stochastic nature of the model does not preclude the accurate determination of structural characteristics of the system. In particular, the interface areas between the three phases can be calculated from the parameters of the model (see Appendix *A*). The values are plotted in Fig. 6. In the course of the temperature-induced dewetting process, the contact area between the solid and phase *A* passes from 0 to about 80 $m^2\ cm^{-3}$. Over the same temperature interval the contact area between phases *A* and *B* decreases by a factor larger than two, from more than 200 $m^2\ cm^{-3}$ to less than 100 $m^2\ cm^{-3}$.

Moreover, when discussing Fig. 4 qualitatively we mentioned that the slope of the A/B boundary line in the (Y, Z) plane controls the *A* or *B* phobicity of the solid phase. This observation can be made quantitative through the calculation of an average contact angle θ_{AS} between the solid and phase *A* (see Appendix *B*). The latter angle is plotted in Fig. 6. It passes from 0° (complete wetting) to about 50° in the course of the wetting transition. These nanometre-scale contact angles may differ significantly from the macroscopic angles that would be measured over a flat surface chemically equivalent to the solid phase of the RF gel (de Gennes *et al.*, 2003; Delmas *et al.*, 2011).

Yet a third interesting structural characteristic of the investigated systems is the specific length L_t of the triple line where phases *A*, *B* and *S* touch each other. The expression of L_t in terms of the other parameters of the plurigaussian model is given in Appendix *B* and the values obtained from the SAXS data are plotted in Fig. 6. The length of the triple line increases steeply when the temperature is decreased. The values of L_t are huge; the order of magnitude is $10^{10}\ m^2\ cm^{-3}$, as expected for nanometre-scaled systems. It has been hypothesized by some authors that there is a thermodynamic cost associated with a triple line, which would take the form of a triple-line tension. However, we are not aware of any experimental procedure to measure L_t in nanomaterials beside the approach we propose here. We hope that our small-angle scattering methodology can contribute to improving our understanding of that interesting problem.

Our results and methodology have to be taken with the same caveat as any small-angle scattering study. Indeed, distinctly different nanostructures may in principle be compatible with a given experimental scattering pattern (Gommes *et al.*, 2012*a*,*b*). This geometrical ambiguity is traditionally tackled using neutron scattering with contrast variation or through anomalous SAXS (Goerigk *et al.*, 2003). These two techniques enable one to obtain information on the individual correlation functions $P_{AA}(r)$, $P_{BB}(r)$ and $P_{SS}(r)$ rather than only on their linear combination as in equation (6). In the present context, however, it is known from direct electron microscopy that clipped GRFs are very accurate models for the structure of empty RF gels. Therefore, the only significant uncertainty in the reconstruction is on the pore-filling phases. It could be argued that the very confinement of the latter phases inside the pores of a known material constitutes a strong geometrical constraint that reduces the ambiguity of the reconstruction.

It is beyond the scope of the present paper to analyze in depth the physical origin of the observed wetting transition. However, the values of the interface areas reported in Fig. 6 provide some insight about the driving force of the process. A macroscopic nitrobezene/hexane solution has an upper critical temperature at 293.5 K (Chen *et al.*, 1983). Two distinct phases would therefore not coexist at 303 K if it were not for a difference in the dispersive forces exerted by the solid phase on nitrobenzene and hexane molecules. The nitrobenzene-rich phase *A* can therefore be viewed as merely a region of space where nitrobenzene molecules concentrate under the influence of dispersive forces exerted by the solid, rather than as a thermodynamic phase. Accordingly, there is no surface tension associated with the nitrobenzene/hexane interface at that temperature. However, this is no longer true when the temperature is decreased: below the critical temperature there is a thermodynamic cost to a nitrobenzene/hexane interface, which drives the system to a configuration with a smaller interface area. This is achieved *via* the dewetting process itself, as well as *via* the coarsening process through which the nitrobenzene plugs grow fewer in number and larger in size (as visible in the large scale reconstructions in Fig. 5). The final configuration and the wetting angles result from an equilibrium between the dispersive forces and the surface tension.

The theoretical possibility of wetting transitions in nanopores has been discussed since the early 1990s (Liu *et al.*, 1990; Monette *et al.*, 1992), and substantial indirect experimental evidence has also been reported for its occurrence. For instance, the existence of a wetting layer on the surface of the porous solid was discovered indirectly through the overall enrichment of the pore-filling liquids in one component compared to the supernatant (Sliwinska-Bartkowiak *et al.*, 1997). Recently, the existence of an adsorbed layer above the critical point was also suggested by SANS in the context of supercritical CO_2 adsorption in silica aerogels (Ciccariello *et al.*, 2011*a*,*b*). In addition, SANS studies have been conducted on a variety of porous materials permeated with different binary liquids (Lin *et al.*, 1994; Formisano & Teixeira, 2000; Hellweg *et al.*, 2003; Schemmel *et al.*, 2005). However, in the latter studies the SAS data have been analyzed in terms of general geometrical concepts, such as correlation and chord lengths, which provided only a limited insight. Indirect evidence of morphological transitions in nanoporous glass have also been obtained by NMR (Valiullin & Furó, 2002) and quasi-elastic neutron scattering (Schemmel *et al.*, 2003). In the present study, we were able to reconstruct for the first time the nanostructure of liquid phases confined in nanopores, thereby giving direct evidence for nanometre-scale wetting transitions.

Wetting transitions on flat or structured surfaces have been documented for a long time (Herminghaus *et al.*, 1998; Trice *et al.*, 2007; Bormashenko, 2010), and they are commonly used to practically control the texture of thin films (Lu *et al.*, 2002) or to create regular patterns of nanoparticles on a surface (Favazza *et al.*, 2006). These nanoparticles can in turn be used, for example, to catalyze the growth of carbon nanotubes (Fan *et al.*, 1999), thereby leading to extremely sophisticated nanostructures that are difficult to obtain by any other means.

The present observation of wetting transitions in nanopores offers the prospect of using the same type of hydrodynamic patterning to control the three-dimensional dispersion of nanometre-scaled objects in the pores of complex materials, rather than only on flat surfaces. Moreover, this offers also the prospect of novel stimuli-responsive nanomaterials. Wetting transitions can indeed be triggered thermally as we report here, but other possible stimuli include the pH (Burtovyy & Luzinov, 2008), the pressure (Bormashenko, 2010), electric fields (Mugele & Baret, 2005) or light intensity in the case of semiconductor solids (Arscott, 2011). In all these cases, wetting transitions are expected to dramatically change the connectedness of the various phases, which is a property that is notoriously difficult to control at the nanometre scale.

Beyond the experimental observation of wetting transitions in nanopores, the ramifications of the present work are mostly methodological. Small-angle scattering is one of the very few experimental methods that can be used for *in situ* studies in nanoporous materials at the mesoscopic scale. So far, most small-angle scattering studies have had to be restricted to academic ordered materials owing to the lack of suitable data analysis methods. The availability of data analysis methods to reconstruct the nanostructure of phases in disordered pores should broaden the applicability of SAS to *in situ* studies in materials of practical relevance, thereby contributing to reducing the gap between nanoscience and nanotechnology.

APPENDIX *A*
Two-point correlation functions and specific surface areas of the plurigaussian model

The two-point correlation function of the pore-filling phases is evaluated through equation (3) by developing the Gaussian bivariate distribution as

$$G_g(x_1, x_2) = \sum_{n=0}^{\infty} \frac{g^n}{n!} H_n(x_1) H_n(x_2) \frac{1}{2\pi} \exp\left(-\frac{x_1^2 + x_2^2}{2}\right), \quad (15)$$

where the $H_n(x)$ are Hermite polynomials defined as

$$H_n(x) = (-1)^n \exp\left(\frac{x^2}{2}\right) \frac{\mathrm{d}^n}{\mathrm{d}x^n} \exp\left(-\frac{x^2}{2}\right). \quad (16)$$

Using this development, the two-point correlation function of any phase X can be written as (Lantuéjoul, 2000)

$$P_{XX}(r) = \sum_{n=0}^{\infty} \sum_{p=0}^{\infty} \frac{g_Y(r)^n}{n!} \frac{g_Z(r)^p}{p!} \Theta_{np}(X)^2, \quad (17)$$

with

$$\Theta_{np}(X) = \int_{(y,z)\in D_X} H_n(y) H_p(z) \frac{1}{2\pi} \exp\left(-\frac{y^2 + z^2}{2}\right) \mathrm{d}y\, \mathrm{d}z. \quad (18)$$

The series in equation (17) converges rapidly, except for small values of r for which $g_{Y/Z}(r) \simeq 1$. In practice, about 20 terms are kept in the series and the small-r values are evaluated as

$$P_{XX}(r) \simeq \phi_X - (S_X/4)r, \quad (19)$$

where S_X is the specific surface area of phase X.

The only characteristics of the Gaussian fields Y and Z that matter for the specific surface areas of the various interfaces are the characteristic lengths $l_{Y/Z}$ defined by the small-r behavior of $g_{Y/Z}(r)$ as

$$g_{Y/Z}(r) \simeq 1 - \left(r/l_{Y/Z}\right)^2. \quad (20)$$

In terms of $f_{Y/Z}(q)$ the characteristic lengths are calculated as

$$1/l_{Y/Z}^2 = \tfrac{1}{6} \int_0^{\infty} f_{Y/Z}(q) q^2 4\pi q^2 \, \mathrm{d}q. \quad (21)$$

Note that the value of l_Z defined in equation (20) is consistent with our notation in equation (11).

We show in the supporting information that the specific interface area between any two phases 1 and 2 of a plurigaussian model can be calculated through the following line integral in the (Y, Z) plane:

$$S_{12} = \frac{2}{\pi^{3/2}} \int_{\partial D_{12}} \exp\left(-\frac{y^2 + z^2}{2}\right) \left(\frac{n_Y^2}{l_Y^2} + \frac{n_Z^2}{l_Z^2}\right)^{1/2} \mathrm{d}l, \quad (22)$$

where ∂D_{12} is the common boundary between domains D_1 and D_2, and $n_{Y/Z}$ are two components of the unit vector locally orthogonal to ∂D_{12}.

Using equation (22), the following expressions are obtained for the specific surface areas of the various phases discussed in the main text, in terms of the parameters defined in Fig. 7. The specific area of the A/B interface is

$$S_{AB} = \frac{2^{1/2}}{\pi} \left\{ \left[\frac{\cos(\beta)}{l_Y}\right]^2 + \left[\frac{\sin(\beta)}{l_Z}\right]^2 \right\}^{1/2} \exp\left(-\frac{b^2}{2}\right) \times \left\{1 - \mathrm{erf}\left[\frac{b\cos(\beta) - a}{2^{1/2}\sin(\beta)}\right]\right\}, \quad (23)$$

where $\mathrm{erf}(x)$ is the error function defined as

$$\mathrm{erf}(x) = \frac{2}{\pi^{1/2}} \int_0^x \exp(-t^2)\, \mathrm{d}t. \quad (24)$$

The area of the A/S interface is

$$S_{AS} = \frac{2^{1/2}}{\pi} \frac{\exp(-a^2/2)}{l_Y} \left\{1 - \mathrm{erf}\left[\frac{b - a\cos(\beta)}{2^{1/2}\sin(\beta)}\right]\right\} \quad (25)$$

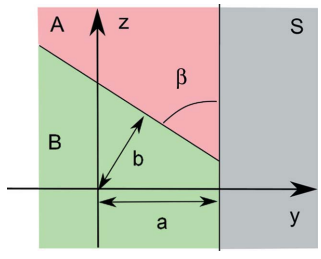

Figure 7
Definition of the (Y, Z) domains of phases A, B and S for the plurigaussian model, and definition of parameters a, b and β.

and the area of the B/S interface

$$S_{BS} = \frac{2^{1/2}}{\pi}\frac{\exp(-a^2/2)}{l_Y}\left\{1 + \operatorname{erf}\left[\frac{b - a\cos(\beta)}{2^{1/2}\sin(\beta)}\right]\right\}. \quad (26)$$

The total specific surface areas of the phases are obtained as $S_A = S_{AS} + S_{AB}$, $S_B = S_{BS} + S_{AB}$ and $S_S = S_{AS} + S_{BS}$. The latter relation in particular leads to

$$S_S = \frac{2^{3/2}}{\pi}\exp\left(-\frac{a^2}{2}\right)\frac{1}{l_Y}, \quad (27)$$

which is the classical expression for the surface area of clipped Gaussian random fields (Berk, 1987).

APPENDIX *B*
Specific length of the triple line and average contact angle

We derive here an expression for the specific length L_t of the triple line at the contact of phases A, B and S, as well as for the contact angle θ between phases A and S, in terms of the parameters of the plurigaussian model.

The general situation is sketched in Fig. 8. For a droplet with a complex shape the wetting angle can only be defined in an average way because it may be variable along the triple line. The average wetting angle can be defined as follows from the area dS of the droplet free surface at a distance smaller than δ from the surface:

$$dS/\delta = L_t/\sin(\theta), \quad (28)$$

where L_t is the specific length of the triple line. In this equation, the left-hand side has to be understood as the ratio of two infinitesimal quantities in the limit $\delta \to 0$. The equivalent of Fig. 8 in the (Y, Z) plane is shown in Fig. 9, in which the surface dS corresponds to the A'/B interface area. We shall now successively calculate (i) the relation between ε and the distance δ in real space, (ii) the length L_t of the triple line corresponding to the contact of phases A', B and S, and (iii) the area of the interface A'/B. We will then be able to calculate the wetting angle θ through equation (28).

B1. Relation between δ and ε

The infinitesimal volume fraction between the iso-surfaces $Y = a$ and $Y = a - \varepsilon$ is, to the first order in ε,

$$d\phi = \frac{\varepsilon}{(2\pi)^{1/2}}\exp\left(-\frac{a^2}{2}\right), \quad (29)$$

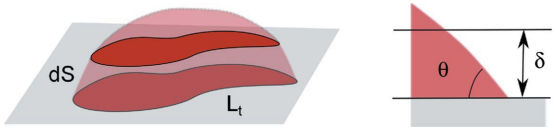

Figure 8
Sketch of a droplet on a flat surface: L_t is the length of the triple line, and dS is the surface area between the solid surface and the plane at distance δ from the surface; θ is the wetting angle.

which results from Y being Gaussian distributed. On the other hand, the same volume is calculated in real space as $d\phi = S_S\delta$, where S_S is the specific surface area of the solid as calculated from equation (27). Equating these two independent estimations of dϕ leads to

$$\delta = (\pi^{1/2}/4)\varepsilon l_Y, \quad (30)$$

which is the relation that we sought between the real-space distance δ and the (Y, Z) plane distance ε.

B2. Specific length L_t of the triple line

The (Y, Z) coordinates of the triple line are (a, c) with

$$c = \frac{b - a\cos(\beta)}{\sin(\beta)}. \quad (31)$$

The specific length of the triple line can be calculated by considering the volume fraction $d^2\phi$ corresponding to a small square in the (Y, Z) plane, centered on the point $Y = a$, $Z = c$, with size ε.

In the (Y, Z) plane, the volume is calculated as

$$d^2\phi = \frac{\varepsilon^2}{2\pi}\exp\left(-\frac{a^2 + c^2}{2}\right) \quad (32)$$

in the limit $\varepsilon \to 0$. On the other hand $d^2\phi$ is calculated in real space as

$$d^2\phi = L_t\delta_Y\delta_Z, \quad (33)$$

where δ_Y and δ_Z and the real-space distances associated with Y and Z differences ε, calculated through equation (30). Equating (32) and (33) leads to

$$L_t = \frac{8}{\pi^2}\exp\left(-\frac{a^2 + c^2}{2}\right)\frac{1}{l_Y l_Z}, \quad (34)$$

which is the relation that we sought between L_t and the parameters of the plurigaussian model.

B3. Interface area dS

Using equation (22), the area dS can be written as

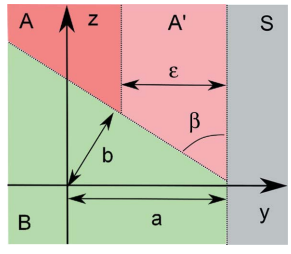

Figure 9
Sub-partitioning of the (Y, Z) plane used to calculate the contact angle. Compared to Fig. 7, a sub-phase A' with extension ε in direction y was added. The reasoning is based on infinitely small values of ε. The thickness of A' was exaggerated for clarity.

$$\mathrm{d}S = \frac{2}{\pi^{3/2}} \exp\left(-\frac{a^2+c^2}{2}\right) \left\{ \left[\frac{\cos(\beta)}{l_Y}\right]^2 + \left[\frac{\sin(\beta)}{l_Z}\right]^2 \right\}^{1/2} \frac{\varepsilon}{\sin(\beta)}. \quad (35)$$

On the other hand, using equation (30) to express δ in terms of ε, and the expression of L_t given in equation (34), the definition of θ [equation (28)] can be written as

$$\mathrm{d}S = \frac{2}{\pi^{3/2}} \exp\left(-\frac{a^2+c^2}{2}\right) \frac{\varepsilon}{l_Z \sin(\theta)}. \quad (36)$$

Equating dS in equations (35) and (36) leads to the simple expression

$$\tan(\theta) = (l_Y/l_Z)\tan(\beta), \quad (37)$$

which is the relation used in the main text to estimate the wetting angle from the SAXS data.

The author is a research associate at the Fonds de la Recherche Scientifique (FRS–FNRS, Belgium). The author is grateful to the Fonds Wetenschappelijk Onderzoek (FWO, Vlaanderen) for supporting the Dutch/Belgian beamline BM26 at the ESRF. The author expresses his gratitude to Dr D. Hermida Merino (BM26), as well as to Mr D. Eskenazi and Mr A. Zubiaur (University of Liège) for their help with the SAXS measurements, and to Professor B. Goderis (University of Leuven) for fruitful discussions.

References

Al-Muhtaseb, S. A. & Ritter, J. A. (2003). *Adv. Mater.* **15**, 101–114.

Armstrong, M., Galli, A. G., Beucher, H., Le Loc'h, G., Renard, D., Doligez, B., Eschard, R. & Geffroy, F. (2003). *Plurigaussian Simulations in Geosciences*. Berlin: Springer.

Arscott, S. (2011). *Sci. Rep.* **1**, 184.

Berk, N. F. (1987). *Phys. Rev. Lett.* **58**, 2718–2721.

Berk, N. F. (1991). *Phys. Rev. A*, **44**, 5069–5079.

Bonnet, F., Lambert, T., Cross, B., Guyon, L., Despetis, F., Puech, L. & Wolf, P. E. (2008). *Eur. Phys. Lett.* **82**, 56003.

Bormashenko, E. (2010). *Philos. Trans. R. Soc. London Ser. A*, **368**, 4695–4711.

Burtovyy, R. & Luzinov, I. (2008). *Langmuir*, **24**, 5903–5910.

Cahn, J. W. (1965). *J. Chem. Phys.* **42**, 93–99.

Chen, C., Herhold, A. B., Johnson, C. S. & Alivisatos, A. P. (1997). *Science*, **276**, 398–401.

Chen, S. H., Lai, C. C., Rouch, J. & Tartaglia, P. (1983). *Phys. Rev. A*, **27**, 1086–1095.

Ciccariello, S., Cocco, G., Benedetti, A. & Enzo, S. (1981). *Phys. Rev. B*, **23**, 6474–6485.

Ciccariello, S., Melnichenko, Y. B. & He, L. (2011*a*). *J. Phys. Chem. C*, **115**, 22336–22346.

Ciccariello, S., Melnichenko, Y. B. & He, L. (2011*b*). *J. Appl. Cryst.* **44**, 43–51.

Ciesla, U. & Schüth, F. (1999). *Microporous Mesoporous Mater.* **27**, 131–149.

Debye, P., Anderson, H. R. Jr & Brumberger, H. (1957). *J. Appl. Phys.* **28**, 679–683.

Delmas, M., Monthioux, M. & Ondarçuhu, T. (2011). *Phys. Rev. Lett.* **106**, 136102.

D'Hollander, S., Gommes, C. J., Mens, R., Adriaensens, P., Goderis, B. & Du Prez, P. (2010). *J. Mater. Chem.* **20**, 3475–3486.

Emma, P. *et al.* (2010). *Nat. Photon.* **4**, 641–647.

Fan, S., Chapline, M. G., Franklin, N. R., Tombler, T. W., Cassell, A. M. & Dai, H. (1999). *Science*, **283**, 512–514.

Favazza, C., Kalyanaraman, R. & Sureshkumar, R. (2006). *Nanotechnology*, **17**, 4229–4234.

Formisano, F. & Teixeira, J. (2000). *J. Phys. Condens. Matter*, **12**, A351–A356.

Friedrich, H., De Jongh, P. E., Verkleij, A. J. & De Jong, K. P. (2009). *Chem. Rev.* **109**, 1613–1629.

Frisken, B. J., Cannell, D. S., Lin, M. Y. & Sinha, S. K. (1995). *Phys. Rev. E*, **51**, 5866–5879.

Galarneau, A., Lefèvre, B., Cambon, H., Coasne, B., Valange, S., Gabelica, Z., Bellat, J. & Di Renzo, F. (2008). *J. Phys. Chem. C*, **112**, 12921–12927.

Gelb, L. D. (2009). *Mater. Res. Bull.* **34**, 592–601.

Gelb, L. D., Gubbins, K. E., Radhakrishnan, R. & Sliwinska-Bartkowiak, M. (1999). *Rep. Prog. Phys.* **62**, 1573–1659.

Gennes, P.-G. de, Brochard-Wyart, F. & Quéré, D. (2003). *Capillarity and Wetting Phenomena: Drops, Bubbles, Pearls, Waves*. New York: Springer.

Glatter, O. & Kratky, O. (1982). *Small-Angle X-ray Scattering*. New York: Academic Press.

Goerigk, G., Haubold, H.-G., Lyon, O. & Simon, J.-P. (2003). *J. Appl. Cryst.* **36**, 425–429.

Gommes, C. J. (2012). *Langmuir*, **28**, 5101–5115.

Gommes, C. J. & Goderis, B. (2010). *J. Appl. Cryst.* **43**, 352–355.

Gommes, C. J., Jiao, Y. & Torquato, S. (2012*a*). *Phys. Rev. Lett.* **108**, 080601.

Gommes, C. J., Jiao, Y. & Torquato, S. (2012*b*). *Phys. Rev. E*, **85**, 051140.

Gommes, C. J., Job, N., Pirard, J.-P., Blacher, S. & Goderis, B. (2008). *J. Appl. Cryst.* **41**, 663–668.

Gommes, C. J., Pirard, J. P. & Goderis, B. (2010). *J. Phys. Chem. C*, **114**, 17350–17357.

Gommes, C. J. & Roberts, A. P. (2008). *Phys. Rev. E*, **77**, 041409.

Häkkinen, H., Abbet, S., Sanchez, A., Heiz, U. & Landman, U. (2003). *Angew. Chem. Int. Ed.* **42**, 1297–1300.

Hänggi, P. & Marchesoni, F. (2009). *Rev. Mod. Phys.* **81**, 387–442.

Harish, R., Karevski, D. & Schütz, G. M. (2008). *J.Catal.* **253**, 191–199.

Hellweg, T., Schemmel, S., Rother, G., Brûlet, A., Eckerlebe, H. & Findenegg, G. H. (2003). *Eur. Phys. J. E*, **12**, 1–4.

Henzler, K., Rosenfeldt, S., Wittemann, A., Harnau, L., Finet, S., Narayanan, T. & Ballauff, M. (2008). *Phys. Rev. Lett.* **100**, 158301.

Herminghaus, S., Jacobs, K., Mecke, K., Bischof, J., Fery, A., Ibn-Elhaj, M. & Schlagowski, S. (1998). *Science*, **282**, 916–919.

Hofmann, T., Wallacher, D., Huber, P., Birringer, R., Knorr, K., Schreiber, A. & Findenegg, G. H. (2005). *Phys. Rev. B*, **72**, 064122.

Jinnai, H., Hashimoto, T., Lee, D. & Chen, S.-H. (1997). *Macromolecules*, **30**, 130–136.

Job, N., Théry, A., Pirard, R., Marien, J., Kocon, L., Rouzaud, J., Béguin, F. & Pirard, J. (2005). *Carbon*, **43**, 2481–2494.

Joshi, M. Y. (1974). PhD thesis, University of Kansas, USA.

Koch, M. H. J. & Bras, W. (2008). *Annu. Rep. Prog. Chem. Sect. C*, **104**, 35–80.

Kusmin, A., Gruener, S., Henschel, A., Holderer, O., Allgaier, J., Richter, D. & Huber, P. (2010). *J. Phys. Chem. Lett.* **1**, 3116–3121.

Lantuéjoul, C. (2000). *Geostatistical Modelling*. Berlin: Springer.

Le Loc'h, G. & Galli, A. (1999). *Geostatistics Wollongong 96 – Proceedings of the Fifth International Geostatistics Congress, Wollongong, Australia, September 1996*, pp. 211–222. Wollongong: Kluwer Academic Publishers.

Lebold, T., Jung, C., Michaelis, J. & Brauchle, C. (2009). *Nano Lett.* **9**, 2877–2883.

Lefort, R., Duvail, J. L., Corre, T., Zhao, Y. & Morineau, D. (2011). *Eur. Phys. J. E*, **34**, 71.

Levitz, P. (1998). *Adv. Colloid Interface Sci.* **76**, 71–106.

Lin, M. Y., Sinha, S. K., Drake, J. M., Wu, X., Thiyagarajan, P. & Stanley, H. B. (1994). *Phys. Rev. Lett.* **72**, 2207–2210.

Liu, A. J., Durian, D. J., Herbolzheimer, E. & Safran, S. A. (1990). *Phys. Rev. Lett.* **65**, 1897–1900.

Lu, G., Li, W., Yao, J., Zhang, G., Yang, B. & Shen, J. (2002). *Adv. Mater.* **14**, 1049–1053.
Marco, R. D. & Veder, J. (2010). *Trend. Anal. Chem.* **29**, 528–537.
Mascotto, S., Wallacher, D., Kuschel, A., Polarz, S., Zickler, G. A., Timmann, A. & Smarsly, B. M. (2010). *Langmuir*, **26**, 6583–6592.
Midgley, P. & Dunin-Borkovski, R. E. (2009). *Nat. Mater.* **8**, 271–280.
Mitchell, J. B. A., Legarrec, J. L., Sztucki, M., Narayanan, T., Dikhtyar, V. & Jerby, E. (2008). *Phys. Rev. Lett.* **100**, 065001.
Mitropoulos, A. C., Makri, P. K., Kanellopoulos, N. K., Keiderling, U. & Wiedenmann, A. (1997). *J. Colloid Interface Sci.* **193**, 137–139.
Monette, L., Liu, A. J. & Grest, G. S. (1992). *Phys. Rev. A*, **46**, 7664–7679.
Mugele, F. & Baret, J. (2005). *J. Phys. Condens. Matter*, **17**, R705–R774.
Neimark, A. V. & Ravikovitch, P. I. (2001). *Microporous Mesoporous Mater.* **44–45**, 697–707.
Nguyen, T. X., Jobic, H. & Bhatia, S. K. (2010). *Phys. Rev. Lett.* **105**, 085901.
Okamoto, K., Shook, C. J., Bivona, L., Lee, S. B. & English, D. S. (2004). *Nano Lett.* **4**, 233–239.
Ouattara-Brigaudet, M., Berthon-Fabry, S., Beauger, C., Chatenet, M., Job, N., Sennour, M. & Achard, P. (2012). *Int. J. Hydrogen Energy*, **37**, 9742–9757.
Pekala, R. W. & Schaefer, D. W. (1993). *Macromolecules*, **26**, 5487–5493.
Powell, M. R., Cleary, L., Davenport, M., Shea, K. J. & Siwy, Z. S. (2011). *Nat. Nanotechnol.* **6**, 798–802.
Quiblier, J. A. (1984). *J. Colloid Interface Sci.* **98**, 84–102.
Quintanilla, J. A. & Jones, W. M. (2007). *Phys. Rev. E*, **75**, 046709.
Roberts, A. P. (1997). *Phys. Rev. E*, **55**, R1286–R1289.
Rolison, D. R. (2003). *Science*, **299**, 1698–1701.
Schaefer, D. W., Pekala, R. & Beaucage, G. (1995). *J. Non-Cryst. Solids*, **186**, 159–167.
Schemmel, S., Akcakayiran, D., Rother, G., Brulet, A., Farago, B., Hellweg, T. & Findenegg, G. H. (2003). *Mater. Res. Soc. Symp. Proc.* **790**, 215–220.
Schemmel, S., Rother, G., Eckerlebe, H. & Findenegg, G. H. (2005). *J. Chem. Phys.* **122**, 244718.
Schoonheydt, A. & Weckhuysen, B. M. (2009). *Phys. Chem. Chem. Phys.* **11**, 2794–2798.
Simonsen, S. B., Chorkendorff, I., Dahl, S., Skoglundh, M., Sehested, J. & Helveg, S. (2010). *J. Am. Chem. Soc.* **132**, 7968–7975.
Simonsen, S. B., Chorkendorff, I., Dahl, S., Skoglundh, M., Sehested, J. & Helveg, S. (2011). *J. Catal.* **281**, 147–155.
Sinha, S. (1999). *Methods of the Physics of Porous Media*, Experimental Methods in the Physical Sciences, Vol. 35, edited by P.-Z. Wong, ch. 6. San Diego: Academic Press.
Sliwinska-Bartkowiak, M., Sowers, S. L. & Gubbins, K. E. (1997). *Langmuir*, **13**, 1182–1188.
Teubner, M. (1991). *Europhys. Lett.* **14**, 403–408.
Torquato, S. (2000). *Random Heterogeneous Materials*. Heidelberg: Springer.
Trice, J., Thomas, D., Favazza, C., Sureshkumar, R. & Kalyanaraman, R. (2007). *Phys. Rev. B*, **75**, 235439.
Valiullin, R. & Furó, I. (2002). *Phys. Rev. E*, **66**, 031508.
Valiullin, R., Kärger, J., Cho, K., Choi, M. & Ryoo, R. (2011). *Microporous Mesoporous Mater.* **142**, 236–244.
Van Honschoten, J. W., Brunets, N. & Tas, N. R. (2010). *Chem. Soc. Rev.* **39**, 1096–1114.
Wallacher, D., Künzner, N., Kovalev, D., Knorr, N. & Knorr, K. (2004). *Phys. Rev. Lett.* **92**, 195704.
Zhang, L., Chmelik, C., Van Laak, A. N. C., Kärger, J., De Jongh, P. E. & De Jong, K. P. (2009). *Chem. Commun.* pp. 6424–6426.
Zhang, X., Lew, K., Nimmatoori, P., Redwing, J. M. & Dickey, E. C. (2007). *Nano Lett.* **7**, 3241–3245.